Experimental Study of Micro-bubble Drag Reduction Using Particle Image Velocimetry

Y. A. Hassan and J. Ortiz-Villafuerte

Department of Nuclear Engineering
Texas &M University
MS 3133
College Station, Texas 77843-3133
Phone: 979 845 7090
Fax: 979 845 6443
Email: y-hassan@tamu.edu

ABSTRACT

Drag reduction was studied when micro-bubbles with low void fractions were injected in the boundary layer of a turbulent channel flow. The particle tracking velocimetry (PTV) flow measurement technique was used to measure velocity fields. Data sets of flow images were acquired to obtain Reynolds-averaged quantities and monitor the flow dynamics. Micro-bubbles, with average diameter of 30 μm, were generated via an electrolysis process using a 76 μm platinum wire with high voltage.
Drag reductions were realized with small void fractions. Similarities with results obtained from drag reduction due to addition of surfactants and polymers as the thickening of the buffer zone, and upward shifts of the logarithmic region were observed. The present results support the theory of an interaction of micro-bubbles with turbulence in the buffer zone, as a mechanism leading to the drag reduction.

1. INTRODUCTION

Drag friction reduction due to injection of micro-bubbles into the boundary layer of a turbulent flow has been known for several years, but the physical mechanism leading to such phenomenon is not totally yet understood. As with other drag reduction technologies, the purpose of micro-bubble injection is to alter the structure of the boundary layer. Micro-bubble injection as drag reduction method in liquid transport has several advantages. For example, fluid separation can be achieved by simply using the density difference between the liquid and gas. If air is chosen to form the micro-bubbles, it can be released without any environmental consequences. Further, mass and heat transfer augmentation by the presence of bubbles in the boundary layer is a well-known phenomenon. Such increase of mass and heat transfer is due to a larger interfacial area available, as well as, a better mixing process.

A large number of experimental, theoretical, and numerical studies have been carried out show the drag reduction by the addition of surfactants and polymers. The literature is rich with this subject, and only some few recent papers will be referenced here. For example, Warholic *et al.* (1999) obtained drag reductions from 10 to 69% by adding different concentrations of polymers to a channel flow with a Reynolds number of about 20000. Advanced surfaces have shown a smaller capability as drag reduction method, usually in the range form 4 to 8% (Lee & Lee 2001), when compared to a flat smooth surface. Other methods known for boundary layer control, and consequently drag reduction, are wall oscillation, and flow suction/injection through the wall.

The injection of microbubbles into the boundary layer has yielded drag reductions larger than 80% on a flat plate (Madavan *et al.* 1985), up to 40% (Kodama 1998) in channel flow. On large scale ships, Takahashi *et al.* (1999) measured skin friction reduction up to 50% on the bottom of a 12 m long ship, while Takahashi *et al.* (2000) up to 32% on a 50 m long ship. By combining polymers and microbubbles, Fontaine *et al.* (1999) achieved drag reductions greater than 80%. However, it is not clear yet the optimum void fraction for drag reduction, or the influence of the size and distribution of the micro-bubbles on the overall process. Such parameters are important in liquid transport in pipes, since high void fraction might lead to bubble coalescence, and then the large bubbles would move towards the pipe center. Thus, instead of achieving power savings, the pressure drop through the pipe length would be higher. One motivation for the present work was to examine the influence of low void fraction microbubbles on the drag reduction.

However the success of achieving large reductions of wall friction depends on understanding the physical mechanism responsible for the friction drag reduction, which is still not fully understood. For the case of polymer addition, experiments indicate that the polymer molecules modify the turbulence structure, by damping the small eddies (Schlichting & Gersten 2000). This phenomenon mainly occurs at the transition zone from the pure viscous sublayer to the overlap layer. The eddy-polymer interaction results in a modification of the turbulent energy cascade (Bhat *et al.* 2000). Microbubbles also interact with eddies in the transition zone, and increase the local dynamic viscosity. This leads to a further increase of the viscous sublayer. It is considered, further, that the microbubble size and distribution are major issues related to the physical mechanism of drag reduction (Kodama 1998), but there is not a single study that demonstrates most of these aspects.

The goal of present paper is to help to improve the understanding of the mechanism leading to drag reduction in a boundary layer, when micro-bubbles are injected. This experimental investigation is focused on the modification of the flow field of a liquid flow when micrometer-size hydrogen bubbles are injected in the turbulent boundary layer. Therefore, it is necessary to use a technique that allows determining simultaneously the liquid flow velocity field, and the size and distribution of the microbubbles injected. Particle image velocimetry (PIV) and its derivatives particle tracking velocimetry (PTV) and shadow image velocimetry (SIV) are good candidates for this type of flow field measurements (Adrian 1991). The capability of PIV in the study of drag reduction with microbubble injection has gained preliminary results by Kakugawa *et al.* (1999).

First, in this study, the boundary layer characteristics of a rectangular channel is studied Micro-bubbles, whose average diameter of 30 μm, were generated via an electrolysis process, using a 76 μm platinum wire with high voltage. A description of the flow facility, and the data acquisition system is also presented. The modification of the flow structure in the boundary layer due to injection of microbubbles is identified. Mean and turbulent flow fields are determined, and the resulting change on the skin friction coefficient is evaluated. The drag reduction results achieved at different low local void fractions are identified. Mean flow parameters and their relation to drag reduction are discussed.

2. EXPERIMENTAL SET-UP AND EXPERIMENTAL TECHNIQUE

2.1 Flow Facility

The flow system consists of a water channel, pumps, flow meters, water filters, two water supply tanks, valves, and fittings. A schematic of the flow system used for this experimental study is shown in figure 1. One of the supply tanks is located above the channel level. In normal operation, the water supply pumped into the upper tank exceeds the flow that can be delivered to the channel through a 2.54 cm hose, and thus, it ensures a constant pressure head. When full, it provides a constant water column of 3.65 m. Its capacity is 0.21 m^3. This tank is also used as phase separator, to avoid air flowing into the channel to assure a single-phase water flow. The other tank is below the channel, as shown in figure 1. Its capacity is 0.35 m^3. This tank receives the overflow from the upper tank, and it is also used to mix the seed tracer particles with the flow.

The channel is made of 12.7 mm thick Plexiglas. Its length is 3.05 m, and the cross section is 0.150 m × 0.0881 m. Nozzles are placed at both ends to allow production of a two-dimensional flow. The inlet nozzle has plastic screens and flow straighteners To ensure a uniform flow. These screens are 6 mm i.d. The mesh size for the screens is about 1.5 mm^2. A multi-layer filters are used to obstruct any particles larger than 10 μm. Prior to start of each test, the water is allowed to flow through the filter, to assure that only the seed tracers will be flowing during the measurements.

The maximum flow currently achievable is 1.02×10^{-3} m^3/s, so the maximum averaged cross section velocity,

$$u_m = \frac{Q}{A}, \qquad \text{Eq. (1)}$$

is 7.72×10^{-2} m/s.

Two Platinum (Pt) wires with a diameter of 76 μm were located about 1 cm from the channel upper wall. These wires serve as cathode and anode for microbubble generation by electrolysis. The first wire is located at a distance of 35.56 cm from the middle of the measurement area. The second wire, the anode, was at 11.43 cm from the middle of the measurement area. The influence of the Pt wires on the flow is negligible, since the Reynolds number based on the wire diameter is less than 10, and the wire is located more than 100000 diameters from the measurement zone.

2.2 PIV system

The PIV system consists of a high power laser, a high resolution CCD camera, a high accuracy pulse generator, and acquisition boards and software. The illumination source for the PIV system is a dual oscillator Nd:YAG laser. Each resonator has a fixed frequency of 30 Hz. It is possible, therefore, to run the laser system at 60 Hz. The maximum power is rated at 400 mJ per pulse, for the 532 nm wavelength (corresponding to green light), but the actual maximum output power achievable range is from 300 to 350 mJ per pulse. The pulse width is about 7 ns.

Two-dimensional PIV images are acquired by a high resolution CCD camera. The camera resolution is 10 bits, 1016 × 1016 pixel, and it runs at 30 Hz. This camera has a 1-inch CCD array format, and the pixel size is 9 μm. This CCD camera has the Trigger Double Exposure capability, which allows for high velocity flow studies.. Since the laser oscillators are fixed at 30 Hz each, a pulse generator is utilized to fire each lamp at the desired time, and with the required time separation between pulses. A four channel digital delay/pulse generator with range of picoseconds is used.

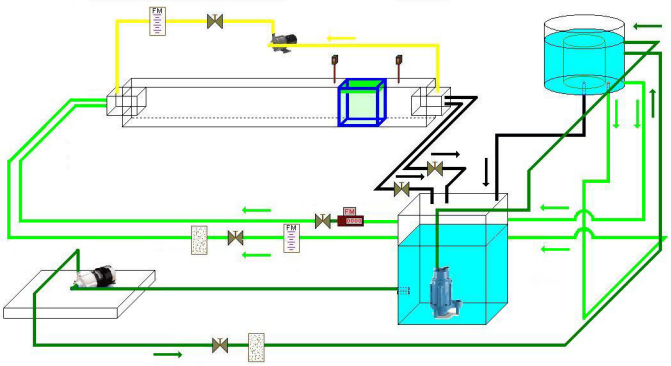

Fig. 2. Flow facility

Fig.1. Flow facility

3. DATA PROCESSING

3.1 Vector Filtering and Analysis

In this study, the particle tracking is a cross correlation algorithm. Two different software applications were used for the tracking process. The resulting velocity vectors from each application were then compared and combined. This hybrid tracking technique greatly increased the total number of velocity vectors used for the flow field analysis. The first software allows for online image processing and tracking of the particle tracers (Uemura et al. 1991). Thus, the image threshold and tracking parameters can be correctly set for a whole data set. This program is considered robust and reliable in particle centroid determination and tracking. The other tracking program and particle centroid determination algorithm are home developed routines (Hassan *et al*. 1992), and they have been improved over the years.

Once the velocity vectors are obtained from both particle-tracking algorithms, they undergo a filtering process. The filters are applied independently to the vector data sets from each tracking process. The first filter is the cross correlation value itself. In our case, only those vectors with a cross correlation coefficient value higher than the average value, sometimes minus a standard deviation, of a whole vector data set are considered for the flow field analysis. In this step usually about 50% of the total vectors are removed. Some of these vectors can easily be seen as erroneous vectors. They are vectors with direction and/or magnitude far deviated from the neighbors. The second filter function is removing vectors that are not within the average +/- a standard deviation value of the magnitude and direction of the representative velocity vector in a small window. This step ensures that velocity gradients are correctly delineated. Then, those vectors close to the image boundaries are also removed. In this step about 10% of the vectors are removed. In total, only about 40% of the initially tracked vectors were kept for analysis after the filtering process. Finally, the remaining vectors from each process are combined to one single file, where they are compared to remove repeated vectors.

3.2 Boundary Layer Tracking Regions

To better resolve the high velocity gradient of the boundary layer, the viewing zone was divided into four regions. The flow fields for single and two phase flows were divided into four regions, to resolve the high velocity gradient of the boundary layer. Each image was divided into four strips in the *y*-direction for the tracking process. Region 1 is from 0 to 100 pixels; region 2 is from 101 to 300 pixels; region 3 is from 301 to 850 pixels and region 4 is from 851 to 1012 pixels. The accuracy of velocity vector determination in region 1 and region 2 are crucial because the velocity field in these regions determine the wall friction velocity. Once the velocity vectors from the hybrid-tracking scheme are filtered, all the instantaneous velocity fields in a set are added in a single data file. The velocity vector accurate positions from the wall are determined. This y-coordinate from the wall is important in the computation of the wall friction velocity.

The mean velocity, $\overline{\mathbf{U}} = \overline{\mathbf{U}}(\overline{U},\overline{V})$, and turbulent velocity , $\mathbf{u} = \mathbf{u}(u,v)$ fields are calculated from the Reynolds decomposition relation.

4. CHARACTERIZATION OF THE BOUNDARY LAYER IN SINGLE PHASE FLOW

Prior to the investigation the physical mechanism of wall friction reduction by injection of microbubbles into the boundary layer, a single phase boundary layer flow is pursued. Water channel flow has been extensively studied and the velocity field for both laminar and turbulent flows are documented. In this study, the single phase measurements consisted of 10 image data sets. Each set was composed of 100 consecutive 1008 × 1012 pixel, 8-bit images. Thus, total of 500 velocity fields could be obtained. However, because not all the images satisfied the minimum quality necessary for image processing, about 450 velocity fields were used for the final data analysis.

4.1 Experimental Conditions

The mean cross sectional velocity given by equation (1) was 7.72 cm/s. The Reynolds number (Re) corresponding to this velocity is 3400.9, based on the half height of the channel. Based on the hydraulic diameter, Re was 8569.9. The values of the density ρ and kinematic viscosity ν were set to 1000 kg/m^3 and 1×10^{-6} m^2/s, respectively. The view area was set to 1.05 cm^2. The time separation between images was 1 ms. The pixel to mm conversion factor was 95.67. The center of the measurement area was located 45.88 cm from the exit nozzle, and 205.62 cm from the inlet nozzle. Thus, the measurement zone was located at L/H = 23.34.

4.2 Average Velocity Field

An average of 22660 velocity vectors per set were used to calculate the mean velocity profile within the measurement zone. Each point on the plot was computed by averaging all the velocity vectors that fall in regions of 1008 × 20 pixel, with 50% overlapping along the *y*-direction. From the average of 10 mean velocity profiles from each data set, it was determined that the boundary layer size was about 7.5 mm. This is based on the premise that at such position the mean velocity reached 99% of the velocity outside the boundary layer that is $\delta_{99} \approx 7.5$ mm. The external velocity was considered to be the mean cross section velocity of 7.72 cm/s.

4.3 Wall Friction Velocity

Friction drag reduction measurements require the wall shear stress τ_w is either directly measured or calculated from the pressure drop, or the wall friction velocity u_τ. Once τ_w is known, the skin friction coefficient C_f for the cases with drag reduction and without drag reduction can be compared. C_f is calculated from

$$C_f = \frac{\tau_w}{\frac{1}{2}\rho u_m^2}, \qquad \text{Eq. (2)}$$

which is equivalent to

$$C_f = 2\left(\frac{u_\tau}{u_m}\right)^2. \qquad \text{Eq. (3)}$$

The use of hot film probes or hot wires is common for the measurement of wall shear stress, but they may induce disturbances to the flow, especially close to the wall. In this particular test, pressure transducers, absolute or differential,

or hot wires or films could not be employed because the high voltage needed for the electrolysis process introduced high intensity noise. Thus, it was not possible to discriminate the noise from the actual pressure transducer signals.

For duct flow, the Blassius equation for the friction factor can be used to calculate u_τ as a first approximation, since C_f is a function of Re. The relationship between C_f and Re for a channel flow is given by

$$C_f = 0.073\,\mathrm{Re}_m^{-1/4}, \qquad \text{Eq. (4)}$$

where

$$\mathrm{Re}_m = \frac{2H u_m}{\nu}, \qquad \text{Eq. (5)}$$

which in this test was 6801.8. Thus, u_τ = 4.89 mm/s. Then, all the data points that fall in the viscous sublayer can be used to determine the actual u_τ.

The major problem in calculating u_τ from velocity measurements within the viscous sublayer is that very few data points can be obtained. In addition due to closeness to the wall, the measurement uncertainty can be high. To avoid this problem, Durst *et al*. (1996) have proposed a more reliable method to estimate u_τ. This method relies on expanding the fluctuating components of the velocity vectors with a Taylor series to approximate the Reynolds stress in near wall region, and then substituting this approximation in the momentum equation. In our case, the Durst's method reduces to

$$\overline{U}^+ = y^+ - \frac{1}{2R^+} y^{+2}. \qquad \text{Eq. (6)}$$

The Blassius or the Power law can be used to give a first approximation of u_τ, and then iteration is employed for each point that satisfy $y^+ \le 12$, until u_τ converges. Then, an average value of u_τ can be calculated.

5. MICROBUBBLE GENERATION

Microbubble size is a parameter influences the gains in drag reduction. Thus, techniques that allow controlling the microbubble size are very desirable. Since high void fractions are normally required, large amounts of gas have to be pumped into or produced inside the duct. Usually, gas is pumped through porous plates. The porous size is commonly of few microns, but the mean microbubble size generated is larger or about 100 μm, and the size can reach up to 1 mm. The bubble size also depends on the liquid velocity.

An alternative to pumping gas through a porous medium to generate microbubbles, they can be generated inside the channel by electrolysis. In this case, the microbubbles are generated on the surface of a metallic wire, through which high voltage or current is applied. In general, the maximum size of the generated microbubbles is that of the wire diameter. The microbubble size decreases with increasing the liquid flow. In addition, microbubbles can be generated continuously or by pulsing the energy source. In this study, electrolysis is used as an effective way to generate and control the size of the microbubbles and to be injected into the desired position within the boundary layer.

A small test facility was built to determine the optimum wire diameter and separation between the cathode and anode. Platinum was chosen because it can handle high voltages and currents, and it is practically corrosion free. The purity of the metal is 99.9%. Two wire diameters of 250 μm and 76 μm were tested. When the voltage source delivers its high voltage (~30000 V), Hydrogen bubbles are produced on the anode, while Oxygen bubbles are generated on the cathode. The anode produces a higher bubble density than the cathode, and the bubbles are smaller. The 76 μm diameter wire was chosen to produce the microbubbles. This is because it produces smaller microbubbles and the bubble concentration density is about the same for both diameters. Figure 2 shows that about 60% of the generated microbubbles had a diameter less or equal to 40 μm at liquid velocity of 10 mm/s, with two main peaks at 26.6 μm and 30.4 μm. This study involved higher flow rate , consequently, the expected microbubble size generated by electrolysis had a peak at about 30 μm.

6. TWO PHASE BOUNDARY LAYER

Figure 3 shows an enhanced and inverted typical image of the two phase boundary layer. In this figure, the bubble layer is adjacent to the channel top wall. The microbubbles mainly appeared in the first 5 mm from the wall. This is due to the bubble buoyancy effect. The microbubbles were generated at a distance of 1 cm from the top wall. Ten image data sets were acquired in the same conditions as the single phase case. Although the microbubble production rate was kept constant during all the measurements, there was microbubble accumulation at the channel top wall, as shown in figure 3.

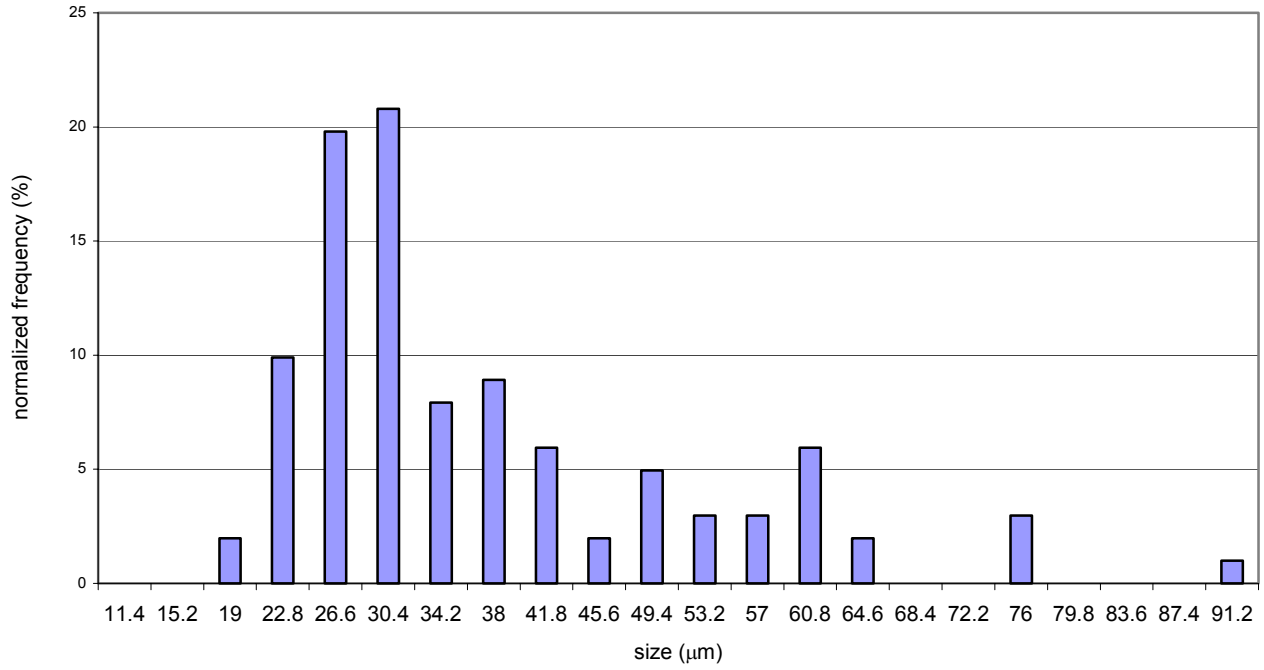

Fig. 2. Microbubble size distribution at a liquid velocity of 10 mm/s

6.1 Tracer Seed and Microbubble Identification

In this study, the differentiation between seeds and microbubbles has been performed based on the spot image size, and the average gray level intensity. The bubble layer adjacent to the wall was not considered in the identification and tracking processes by applying a mask to that area. Once the tracer particles and microbubbles were distinguished, instantaneous velocity fields were calculated from the spot image displacements. The filtering and cleaning process was employed on the velocity vectors.

6.2 Void Fraction Calculation

The microbubble size and its spatial distribution within the boundary layer are important parameters in achieving high drag reduction. The size of the scale of the structures responsible for turbulence production should be of the same order as the microbubble diameter for effective interaction. Producing or keeping microbubbles in this layer is required to enhance the drag reduction. The local void fraction can be inferred from microbubble size and spatial distribution within the boundary layer.

The nominal definition of void fraction α is

$$\alpha \equiv \frac{V_g}{V_g + V_l}, \qquad \text{Eq. (7)}$$

where V_g is the volume occupied by the dispersed phase, and V_l the volume occupied by the continuous phase. In most the literature related to drag reduction by microbubble injection, the average void fraction is assumed to be equivalent to the ratio of the volumetric flow rates of the gas to the total flow rates (Madavan *et al*. 1985; Fontaine *et al*. 1999; Kodama *et al*. 2000), which is known as the volumetric quality β, and it is given by

$$\beta = \frac{Q_g}{Q_g + Q_l}, \qquad \text{Eq. (8)}$$

where Q_g is the flow rate of the gas, and Q_l the flow rate of the liquid. In order to determine a more appropriate parameter to relate the gas fraction in the boundary layer to the drag reduction, Madavan et al. proposed that the parameter β be a function of the boundary layer parameters. Thus, they defined the liquid flow rate as a function of the boundary layer thickness δ and the boundary layer displacement thickness δ^*, as

$$Q_l \equiv U_\infty \left(\delta - \delta^*\right) b, \qquad \text{Eq. (9)}$$

where U_∞ is the external velocity to the boundary layer, and b is the width of the porous area they used in their experiments.

It has been shown in several experimental studies that the drag reduction increases as β increases, until a maximum is reached (Madavan *et al*. 1985; Fontaine *et al*. 1999; Kodama *et al*. 2000). Drag reductions as high as 80% were achieved with a value of β (β = 25%) by Fontaine *et al*. However, β was about 40% in the study of Madavan *et al*. for the same 80% drag reduction. Note that two different geometries were employed in the mentioned studies, but similar definitions for Q_l were used. However, since α is not necessarily equal to β, a correlation between α and drag reduction is not clear at present time.

At such high values of β, it is clear that flow visualization techniques cannot yield accurate results about both phase velocity fields, since the microbubbles form layers that obscure the view area. Furthermore, size and spatial distribution of the microbubbles in the boundary layer are difficult to measure under such circumstances with the measurement techniques. For this reason, in this experimental study we have taken a different path, which has not been explored before, to the best of our knowledge. Here, we propose to use very low local void fractions, i.e., less than 5%. Such low void fractions allow the use of the particle image velocimetry technique for measurement of the velocity fields of both dispersed and continuous phases. In principle, both size and spatial distribution of the microbubbles are obtained from PIV data. In this study, the total void fraction in the measurement volume was calculated by adding the contribution of the bubble layer plus the microbubbles freely flowing in the view volume, that is,

$$\alpha = \alpha_{bl} + \alpha_{fb}, \qquad \text{Eq. (10)}$$

where α_{bl} is the void fraction due to the microbubble layer formed at the channel top wall, as shown in figure 3, and α_{fb} is the void fraction due to microbubbles that move with the flow. The first part of α was computed assuming that the bubble layer occupied the volume of a rectangular box V_{bl}, that is,

$$V_{bl} = l \times b \times h, \qquad \text{Eq. (11)}$$

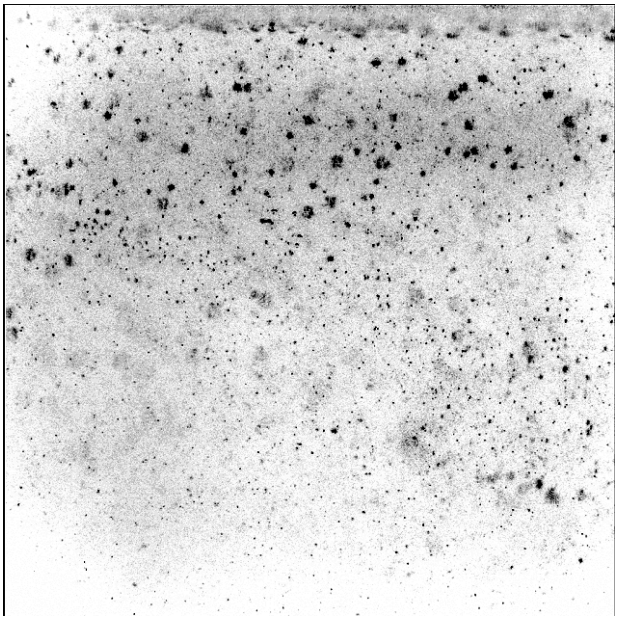

Fig. 3. Typical image from a two phase boundary layer measurement. The image has been enhanced and inverted.

where *l* is the image size along the *x*-direction (1008 pixel = 10.54 mm), *b* is the laser light sheet width (1 mm), and *h* is the bubble layer thickness on the images. This parameter *h* varied from 15 to 63 pixel, and thus, α_{bl} varied from 1.5% to 6.2%. The second contribution, α_{fb}, did not change, in practice, the values just presented, since a maximum of 300 microbubbles could be found on the images. Therefore, practically $\alpha \sim \alpha_{bl}$. However, the distribution of the freely moving microbubbles in the boundary layer, that is, the α_{fb} distribution, proved to be a key parameter on the drag reduction. In this study, the local distribution and shape of α_{fb} in the boundary layer have paramount influence in the drag reduction.

6.3 Distribution of the Freely Moving Microbubbles

Figure 4 shows the α_{fb} distribution versus the distance form the wall *y* for the 10 data sets. The void fraction values shown in the figure are for the total value of α. It can be noted in this figure that the different data sets do not have a common initial point. This reflects the thickness of the microbubble layer. Also, they do not start at a distribution value of zero, but the number of microbubbles at the initial point is low. The distribution of all the sets clearly presents two peaks. The first peak appears just after the bubble layer, and the second peak at about the middle of the measurement area. The first peak is quite narrow compared to the second one, in which a gradual increase and decrease can be seen. It also should be noted that the maximum value of α does not correspond to the highest peaks, and that after 10 mm, the distance from the wall at which the microbubbles were generated, the distribution rapidly falls towards zero.

7. MICROBUBBLE DRAG REDUCTION RESULTS

The realized friction drag reduction is presented as a function of the total void fraction α

Drag Reduction Estimation

In this study, the drag reduction was calculated based on the measurements of the wall friction velocity u_τ. The Durst's method (Durst *et al*. 1996) was used for the calculation of u_τ. To calculate the drag reduction, DR, the ratio of the skin

friction coefficients with microbubbles C_f to that without microbubbles C_{f0} is equal to the ratio of the wall shear stresses with microbubbles τ_w to that and without microbubbles τ_{w0}. The percent drag reduction was calculated from

$$\mathrm{DR} = 100 \times \left[1 - \left(\frac{u_\tau}{u_{\tau 0}} \right)^2 \right]. \qquad \text{Eq. (12)}$$

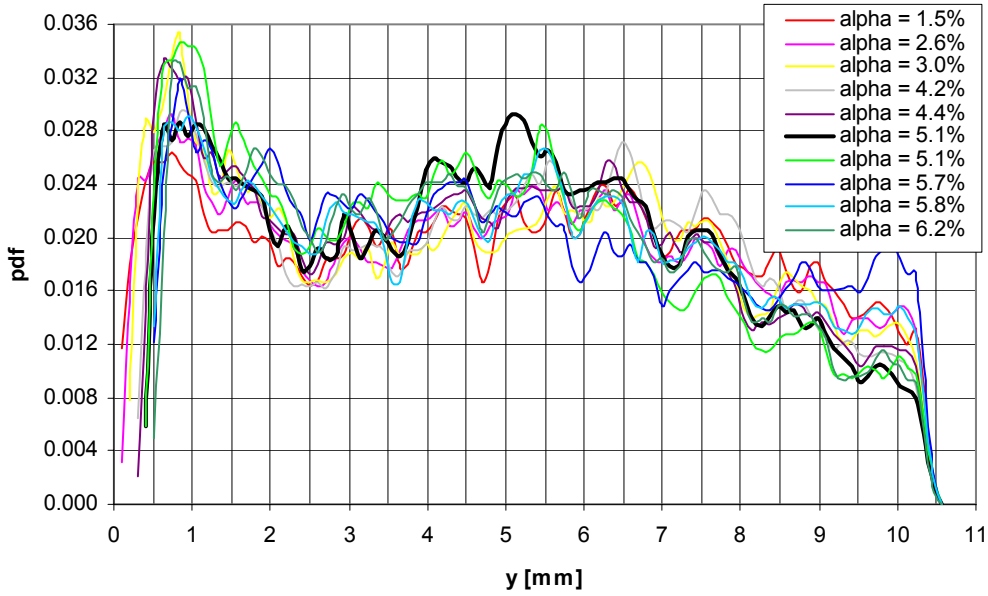

Fig. 4. Distribution of the freely moving microbubbles in the measurement zone for the 10 two phase flow data sets. The alpha value shown refers to the total void fraction, see text.

7.2 Role of the Bubble Distribution in Drag Reduction

It is known that an increase in the void fraction in the boundary layer leads to an increase in drag reduction, until a maximum is reached. However, in this study it the local void fractions of microbubbles that are in the buffer zone are the key parameter in drag reductions. The bubble layer at the top of the channel wall which practically accounts for the total void fraction has insignificant contribution in the drag reduction.

Figure 5 shows that the first peak of the microbubble pdf, which is located in the viscous sublayer, does not play an important role in the drag reduction phenomenon. Figure 6 indicates that although the void fraction profiles are similar, those cases where there is microbubble accumulation in the area from $y^+ \approx 15$ to 30 present higher drag reductions.

It is possible to realize the cause of higher void fractions yielding higher drag reductions. By injecting more microbubbles the probability of getting more bubbles in the buffer zone increases.

Figure 6 shows the effect of the void fraction on the non-dimensional mean velocity u^+ as a function of the y^+ distance. A similar behavior was obtained with surfactants and polymers.

7.3 Uncertainty

The experimental error associated to the present measurements was calculated to be 4.5%. The major impact on the error analysis comes from the uncertainty in determining the particle image centroid, for the tracking process. This error was determined to be 0.1 pixel.

8. CONCLUSIONS

An experimental study of drag reduction using microbubbles as drag reducing agents have been performed. The particle tracking velocimetry technique was employed for the measurement of the velocity fields of both phases. Microbubbles, whose average size was 30 μm, were generated in a turbulent boundary layer of a channel flow.

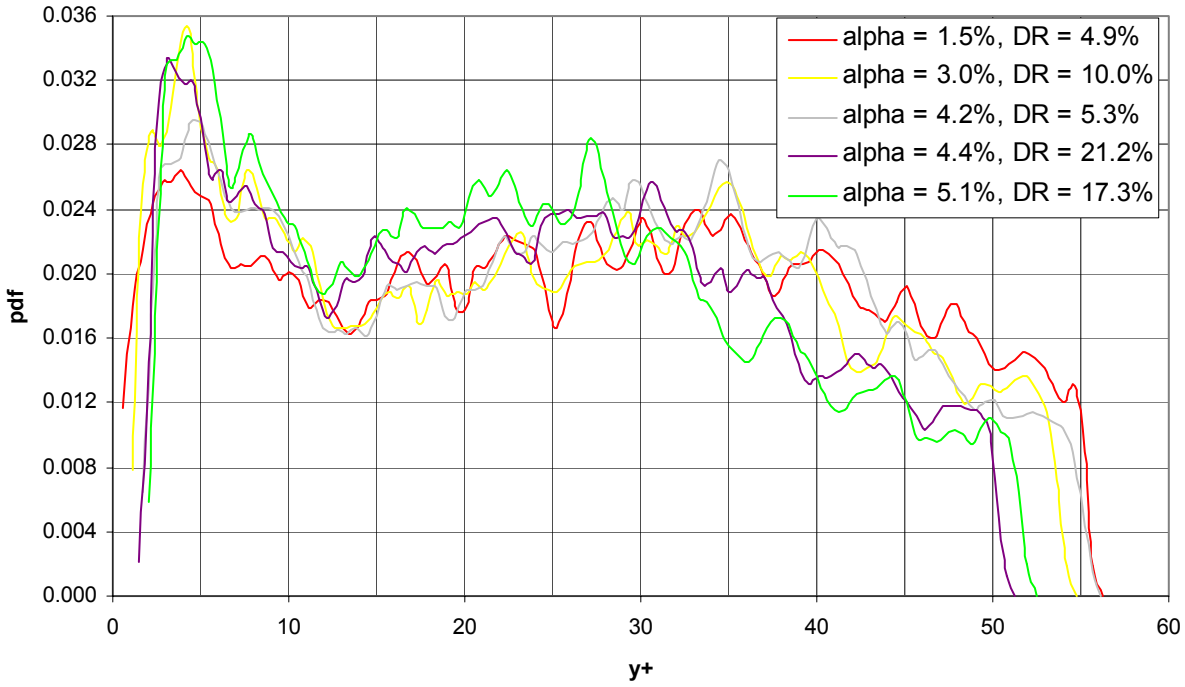

Fig. 5. Distribution of the freely moving microbubbles for five cases of different drag reduction versus the non-dimensional distance from the wall.

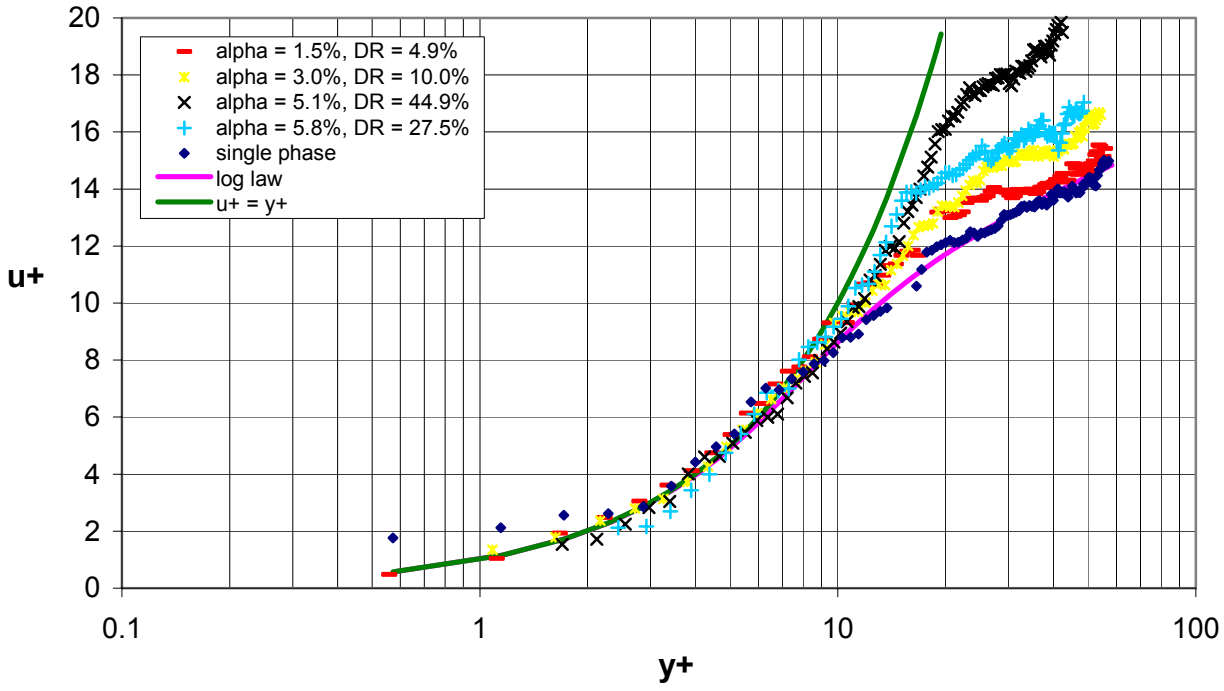

Fig. 6. Mean velocity profiles for four different drag reductions in wall units.

Similarities with results obtained from drag reduction due to addition of surfactants and polymers were observed, as the thickening of the buffer zone, and upward shifts of the logarithmic region. However, noticeable differences were also found. It is the first time, to our knowledge that high drag reductions can be achieved with very low local void fractions. It was also shown that the microbubble layer formed at the top the channel has no major role in drag reduction, but to reduce the slip between liquid and microbubbles. The present data suggest that the most important aspect in achieving high drag reductions is the accumulation of microbubbles in a critical zone in the buffer layer, from $y^+ = 15$ to $y^+ = 30$. It seems that there is a minimum critical microbubble accumulation necessary to achieve drag reductions of about 20% or higher.

The present results support the theory of an interaction of micro-bubbles with turbulence in the buffer zone, as mechanism leading to the drag reduction.

REFERENCES

Adrian R J (1991) Particle-imaging techniques for experimental fluid mechanics. *Annual Rev Fluid Mech* **23**, 261-304.

Bhat S K P; Pal K & Chopra S (2000) A study of intermittency and drag reduction in turbulence by dynamic laser light scattering. *Exp Fluids* **28**, 160-164.

Durst F; Kikura H; Lekakis I; Jovanovic J & Ye Q (1996) Wall shear stress determination from near-wall mean velocity data in turbulent pipe and channel flows. *Exp Fluids* **20**, 417-428.

Fontaine A A; Deutsch S; Brungart T A; Petrie H L & Fenstermacker M (1999) Drag reduction by coupled systems: microbubble injection with homogeneous polymer and surfactant solutions. *Exp Fluids* **26**, 397-403.

Hassan Y A; Blanchat T K; Seeley Jr C H & Canaan R E (1992) Simultaneous velocity measurements of both components of a two-phase flow using particle image velocimetry. *Int J Multiphase Flow* **18**, 371-395.

Kakugawa A; Kawashima H; Takahashi T & Kodama Y (1999) Velocity measurements of flows with microbubbles using PIV. *ATEM'99 JSME*. Ube City, Japan. http://www.srimot.go.jp/spd/drag/drag2e.htm.

Kodama Y (1998) Effect of microbubble distribution on skin friction reduction. *International Symposium on Seawater Drag Reduction.* http://www.srimot.go.jp/spd/drag/drag2e.htm.

Kodama Y; Kakugawa A; Takahashi T & Kawashima H (2000) Experimental study on microbubbles and their applicability to ship for skin friction reduction. *Int J Heat Fluid Flow* **21**, 582-588.

Lee S J & Lee S H (2001) Flow field analysis of a turbulent boundary layer over a riblet surface. *Exp Fluids* **30**, 153-166.

Madavan N K; Deutsch S & Merkle C L (1985) Measurements of local skin friction in a micobubble-modified turbulent boundary layer. *J Fluid Mech* **156**, 237-256.

Schlichting H & Gersten K (2000) *Boundary Layer Theory*. 8th edition, Springer, New York.

Takahashi T; Kakugawa A; Kawashima H & Kodama Y (1999) Experimental skin friction reduction by microbubbles using a ship with a flat bottom. *31st Symposium on Turbulence Flow*. http://www.srimot.go.jp/spd/drag/drag2e.htm.

Takahashi T; Kakugawa A; Makino M; Yanagihara T & Kodama Y (2000) A brief report on microbubble experiments using 50 m-long flat plate ship. *74th General Meeting of SRI*. http://www.srimot.go.jp/spd/drag/drag2e.htm.

Uemura T; Yamamoto F & Ohmi K (1991) Mixing flow in a cylindrical vessel agitated by a bubbling jet. *Application of Laser Techniques to Fluid Mechanics*. Springer-Verlag, 512-536.

Warholic M D; Massah H & Hanratty T J (1999) Influence of drag-reducing polymers on turbulence: effects of Reynolds number, concentration and mixing. *Exp Fluids* **27**, 461-472.